Materials Advances

ROYAL SOCIETY OF CHEMISTRY

PAPER

View Article Online
View Journal

Cite this: DOI: 10.1039/d6ma00117c

Study of the structural, optical, and electronic properties of gadolinium orthophosphate: a combination of experimental and theoretical studies

I. Abdelrhafor, *[a] L. H. Omari, *[ab] M. Lassri,[c] S. Tarik,[a] A. El Hachmi,[d] H. Lassri,[a] E. K. Hlil[e] and E. Dhahri[f]

We present an in-depth study combining experimental techniques with *ab initio* density functional theory (DFT) calculations to elucidate the electronic structure and optical properties of gadolinium orthophosphate ($GdPO_4$). Experimentally, X-ray diffraction (XRD) and Raman spectroscopy were used to characterize the synthesized pure phase of $GdPO_4$. Rietveld refinement analysis confirmed that $GdPO_4$ crystallizes in the monoclinic space group $P2_1/n$ with a monazite structure. UV-visible diffuse reflectance spectroscopy was performed on synthesized $GdPO_4$ powders. The absorption coefficient was analyzed *via* the Kubelka–Munk transformed Tauc plot to explore the optical bandgap value of $GdPO_4$. In addition, the absorption coefficient derived from UV-visible measurement demonstrated two peaks at 275 and 303 nm, corresponding to the 4f–4f transitions $^8S_{7/2} \rightarrow {}^6I_J$ and $^8S_{7/2} \rightarrow {}^6P_{7/2}$ of Gd^{3+}, respectively. Theoretically, DFT+mBJ+SOC was employed to simulate the density of states, band structures, and complex dielectric functions. We also successfully identified both $4f^n$–$4f^n$ and $4f^{n-1}5d^1$ transitions by means of DFT. Our main findings include an accurate prediction of the energy of the possible emitted photon (3.96 eV), which aligns with the experimental measurement of luminescence. Additionally, the predicted electronic bandgap of 7.8 eV for the monazite crystal $GdPO_4$ is consistent with previous experimental data. This large gap is typical for rare-earth orthophosphate systems. The results of our computational study are also validated by magnetic moment estimation. The Gd atom shows a saturation magnetic moment of $6.86\mu_B$, which is congruent with the experimentally measured magnetic moment $\mu_{exp} = 7.2 \pm 0.3\mu_B$.

Received 23rd January 2026,
Accepted 13th April 2026

DOI: 10.1039/d6ma00117c

rsc.li/materials-advances

1. Introduction

Lanthanides, also known as rare-earth elements (REEs), belong to the f-block of the periodic table. They are typically classified into two structural groups based on their phosphate compounds. The orthophosphates of the lighter and larger lanthanides ($LnPO_4$, where Ln = La to Gd) crystallize in a monoclinic monazite-type structure, associated with the space group $P2_1/n$. In contrast, the orthophosphates of the heavier and smaller lanthanides (Ln = Tb to Lu) have a zircon-like tetragonal structure, commonly called xenotime, with the space group $I41/amd$.[1] Lanthanide orthophosphates ($LnPO_4$) are attracting increasing interest due to their unique optical and structural properties, making them promising candidates for various applications, including luminescence-based temperature sensing, optical materials, and energy-related devices,[2,3] and semiconductor lighting devices.[4,5] Monazite-type rare earths (REEs) have been extensively researched for use in various advanced applications, including their use as geochronological microprobes,[6] scintillators for X-ray and gamma-ray detection in medical imaging systems,[7] and host materials in semiconductor lasers.[8] Thanks to their exceptional structural stability and resistance to radiation-induced damage, they are also considered promising candidates for immobilizing minor actinides and plutonium in nuclear waste management strategies.[9,10] Recently, gadolinium-based orthophosphates have attracted considerable interest due to the advantageous electronic properties of 4f elements, including their high magnetic moments

[a] *LPMAT, Faculté des sciences Ain Chock, Université Hassan II de Casablanca, Morocco. E-mail: imaneabdelrhafor@gmail.com, bophysiq@gmail.com*
[b] *LEST Laboratory, ESEF Berrechid, Hassan First University of Settat, Morocco*
[c] *EMINES-SAEP, UM6P, Mohammed VI Polytechnic University, Lot 660, Hay Moulay Rachid, 43150, Ben Guerir, Morocco*
[d] *Physico-chemistry of Materials Team, Faculty of Science, Abdelmalek Essaadi University, Tetouan, Morocco*
[e] *Univ. Grenoble Alpes, CNRS, Grenoble INP, Néel Institute, 38000, Grenoble, France*
[f] *Faculté des Sciences de Sfax, Université de Sfax, 3000, BP 1171, Tunisia*

and rapid electronic relaxation times, on the order of nanoseconds. These properties make them suitable for a wide range of applications, including the labelling of biological and medical samples for *in vitro* imaging.

In particular, $GdPO_4$ has demonstrated superior performance compared to certain commercially available contrast agents.[11] Recently, $GdPO_4$ has been identified as a promising low-temperature magnetic refrigeration material for magnetocaloric applications due to its significant magnetocaloric effect.[12] It also exhibits second-order magnetic phase transition behavior.[12–14] Coating cathode materials with Gd orthophosphates has proven to be a highly effective method for advanced lithium-ion battery applications. In the case of $LiFePO_4$, the incorporation of a $GdPO_4$ layer can significantly improve ionic and electronic conductivity while suppressing undesirable side reactions at the interface between the electrode and the electrolyte.[15] In addition, Ni-rich NCA cathodes coated with $GdPO_4$ exhibit enhanced current density performance and superior capacity retention stability.[16]

In this work, we report on a comparative study of $GdPO_4$, including density functional theory (DFT) calculations and experimental optical measurements. The first part of the study presents the synthesis and structural characterization of $GdPO_4$ using XRD and Raman spectroscopy, followed by optical characterization to identify electronic transitions. The second part will involve the study of the electronic and optical properties using DFT. To ensure reliable and accurate results, we have adopted the GGA+mBJ functional to describe the exchange–correlation potential, in addition to the spin–orbit-coupling (SOC) scheme. The electronic gap energy was predicted alongside an analysis of intra- and inter-configurational transitions. A discussion of points of agreement, similarities, and divergences then followed.

2. Experimental

2.1. Procedure of synthesis

Polycrystalline $GdPO_4$ was prepared using a solid-state reaction method. The raw materials used were high-purity gadolinium oxide (Gd_2O_3, 99.99%) and ammonium dihydrogen phosphate $(NH_4)_2HPO_4$, 99.9%, in stoichiometric proportions. According to the standard protocol, the gadolinium oxide precursor Gd_2O_3 was calcined at 1073 K for 1 hour. After that, a stoichiometric amount of $(NH_4)_2HPO_4$ was then added, thoroughly ground and heated at 1623 K for 12 hours in an alumina crucible. The thermal treatment was repeated once.

2.2. Characterization

Powder X-ray diffraction (PXRD) was utilized to verify the successful synthesis of $GdPO_4$. Measurements were performed using a Bruker D8 diffractometer employing Cu-Kα radiation (λ = 0.15406 nm). The scanning range for 2θ was set from 15° to 80°, with data collected at 0.2° intervals and at a scan speed of 1 second per step. For Rietveld refinement, the established structure of $GdPO_4$, characterized by the $P21/m$ space group, served as the foundational model. The vibrational properties of the synthesized $GdPO_4$ were investigated using Raman spectroscopy. Spectra were recorded in the 300–1350 cm^{-1} range. The UV-vis spectra were recorded *via* a spectrometer/Data System JASCO Corp., V-570, Rev.1.00 in the 250–850 nm wavelength range. All the spectra were recorded at room temperature ($\sim$298 K). The measured sample was 2 millimeters thick. The spectrometer has a wavelength accuracy of $\pm$0.3 nm. The uncertainty over absorbance is 0.13%.

3. Computational methods

In order to investigate the electronic properties, a computational study was conducted using density functional theory (DFT) with the full-potential linearized augmented plane-wave method, as implemented in the Wien2k simulation package.[17,18]

The computational approach involves resolving the Kohn–Sham equations by expanding the wave functions in terms of spherical harmonics within the atomic spheres, while plane-wave expansions are applied in the interstitial regions of the unit cell. For all calculations, the exchange–correlation potential (Exc) was treated using the generalized gradient approximation (GGA) in the Perdew–Burke–Ernzerhof (PBE) formulation.

To obtain an accurate electronic structure, the DFT+mBJ+SOC method was adopted to overcome the well-known shortcoming of GGA.[19] The mBJ method was used to describe the strongly correlated electrons of the Gd^{3+} ion occupying the 4f orbital. Additionally, the 4f electrons of Gd were treated as valence states. The Spin–Orbit Coupling (SOC) had also been added for gadolinium. The muffin-tin radii (RMT) for the three atoms Gd, P, and O were fixed at 2.2, 1.35, and 1.48 Bohr, respectively.[20]

The k-point sampling of the Brillouin zone was performed using 9 $\times$ 9 $\times$ 10 k-mesh grids. The spin-polarized ferromagnetic configuration was included in the calculations self-consistently. The convergence criterion for the self-consistent field of the Kohn–Sham equations was established at 10^{-4} eV.

4. Results and discussion

4.1. Structural properties

4.1.1. X-ray diffraction XRD. The powder X-ray diffraction (PXRD) patterns of $GdPO_4$, recorded at ambient temperature, were successfully indexed using the PDF2 database[21] integrated into HighScore Plus software,[22] and structural analysis *via* the DICVOL program[23] confirmed a single-phase composition consistent with a gadolinium phosphate structure.

The crystal structure of the studied compound was investigated using the Rietveld refinement[24] with the FullProf program,[25] revealing that it crystallizes in the monoclinic system, with the space group $P2_1/n$ (No. 14) and unit-cell parameters a = 6.6532(3) Å, b = 6.8491(3) Å, c = 6.3366(3) Å, and β = 104.001(2)°. The unit-cell volume was determined to be 280.17(2) $Å^3$, with a calculated density of 5.981 g cm^{-3}. The number of formula units per unit cell (Z) is 4. The XRD patterns were correctly indexed by assigning the monoclinic space group $P2_1/n$ (No. 14), for which

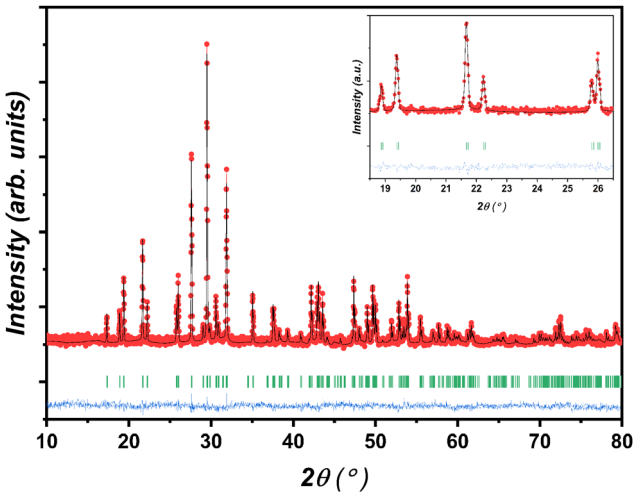

Fig. 1 Rietveld refinement plots of the $GdPO_4$ phase.

the general reflection conditions are: $h0l$: $h + l = 2n$; $0k0$: $k = 2n$; $h00$: $h = 2n$; and $00l$: $l = 2n$, as specified in the International Tables for Crystallography, Volume A: Space-Group Symmetry.[26]

Fig. 1 presents the final Rietveld refinement plot for the $GdPO_4$ compound. Experimental X-ray diffraction data are represented by red dots, while the calculated diffractogram is represented by a solid black line. The positions of Bragg reflections are indicated by green vertical lines. The blue curve at the bottom represents the difference between the observed and calculated intensities. Table 1 presents the crystallographic data, data acquisition details, and refinement parameters, including lattice parameters, unit cell volume, crystal system, space group, and various statistical agreement indices. The reliability factors (%) – R_p = 3.89, R_{wp} = 4.92, R_{exp} = 4.07 – and the goodness-of-fit value χ^2 = 1.47 indicate a high-quality fit, as these values are low. The excellent agreement between the experimental points (dots) and the calculated profile (solid line) in Fig. 1 confirms the accuracy of the refinement. The refined structure meets the criteria for chemical plausibility and statistical robustness. The fractional atomic coordinates and isotropic displacement parameters are presented in Table 2. The Gd^{3+}, P^{5+}, and O^{2-} ions occupy 4-electron sites at positions (x, y, z). A P^{5+} cation is coordinated by four oxygen ions (4-coordination), while a Gd^{3+} ion is coordinated by ten oxygen ions (10-coordination). Table 3 presents the selected diatomic distances (in Å) and bond valences. The average bond lengths ⟨Gd–O⟩ and ⟨P–O⟩ determined by Rietveld refinement are congruent with the predicted bond lengths of 2.5105 Å for Gd^{3+}–O^{2-} and 1.5344 Å for P^{3+}–O^{2-}. The average crystallite size of the compound $GdPO_4$ was estimated by X-ray diffraction line broadening analysis, using the Scherrer equation. It is important to note that X-ray diffraction peak broadening can be due to multiple factors, including crystallite size, macrostrains, instrumental contributions, temperature, and compositional inhomogeneities.

The Scherrer equation is defined as follows:

$$D = \frac{K\lambda}{\beta \cos\theta} \quad (1)$$

where D denotes the average crystallite size (in nanometers), K is the aspect ratio (taken as 0.9), and λ represents the wavelength. In this study, the crystallite size is calculated from the X-ray diffraction pattern using the main peak at approximately $2\theta \approx 29.51^\circ$, resulting in an average crystallite size of

Table 1 Rietveld refinement details for the studied material

Formula	$GdPO_4$
M_r	252.2214
Temperature (K)	300
d_{calc} (g cm^{-3})	5.981
Radiation	Cu-K_α
Wavelengths (Å)	1.54056 (λ_1) 1.54439 (λ_2)
2θ range (°)	10–80
2θ step (°)	0.020283
Program	FullProf
Pseudo–Voigt function: [PV = $\eta L + (1 - \eta)G$]	η = 0.50(6)
Caglioti parameters (u, v, w)	0.022(5), −0.018(4), 0.0095(8)
No. of reflections	374/2
No. of fitted parameters	35
Crystal system	Monoclinic
Space group	$P2_1/n$ (No. 14)
Lattice parameters	a = 6.6532(3) Å, b = 6.8491(3) Å, c = 6.3366(3) Å, β = 104.001(2) °
Cell-volume (Å^3)	280.17(2)
Formula units per unit cell (Z)	4
Reliability factors	R_p = 3.89, R_{wp} = 4.92, R_{exp} = 4.07
Goodness-of-fit (χ^2)	1.47

Table 2 Atomic coordinates and isotropic displacement parameters for the $GdPO_4$ phase

	x	y	Z	B_{iso} (Å^2)	Occ.	Site
Gd^{3+}	0.2798(5)	0.1553(6)	0.0959(6)	0.8(1)	1	4e
P^{5+}	0.296(2)	0.163(2)	0.607(3)	0.6(3)	1	4e
O1	0.252(4)	−0.005(4)	0.418(6)	2.2(4)	1	4e
O2	0.369(3)	0.325(4)	0.508(5)	2.2(4)	1	4e
O3	0.467(4)	0.119(4)	0.816(4)	2.2(4)	1	4e
O4	0.114(4)	0.223(4)	0.714(4)	2.2(4)	1	4e

Table 3 Selected bond lengths (Å) and corresponding bond valences derived from Rietveld refinement

		Distances (Å)	Bond-valences
Gd–O1	(×1)	2.36(4)	0.45(4)
	(×1)	2.34(3)	0.48(4)
Gd–O2	(×1)	2.79(3)	0.14(1)
	(×1)	2.49(3)	0.31(2)
	(×1)	2.66(2)	0.20(1)
Gd–O3	(×1)	2.41(3)	0.39(3)
	(×1)	2.50(3)	0.31(2)
	(×1)	3.17(3)	0.050(4)
Gd–O4	(×1)	2.45(2)	0.35(2)
	(×1)	2.32(3)	0.50(4)
⟨Gd–O⟩$_{average}$, BVS		2.549(9)	3.19(9)
P–O1	(×1)	1.64(4)	0.95(9)
P–O2	(×1)	1.42(3)	1.72(15)
P–O3	(×1)	1.55(3)	1.19(9)
P–O4	(×1)	1.58(3)	1.11(10)
⟨P–O⟩$_{average}$, BVS		1.55(2)	4.97(22)

103 nm. Furthermore, the size of crystallites is directly related to the density of imperfections in the crystal lattice, commonly called dislocation density (δ), which can be estimated using the following relationship:

$$\delta = \frac{1}{D^2} \quad (2)$$

Here, δ denotes the dislocation density, while D is the mean crystallite size. The dislocation density calculated for the sample is 9.357×10^{13} m^{-2}.

4.1.2. Raman spectra. The Raman spectrum of $GdPO_4$ nanoparticles, presented in Fig. 2, reveals a series of distinct vibrational modes characteristic of the phosphate group and the crystalline structure of the compound. Owing to the distinct structural roles of the Gd^{3+} cations and the $(PO_4)^{3-}$ groups in the monazite structure, the crystal can be reasonably approximated as consisting of two interpenetrating sublattices, one formed by Gd^{3+}ions and the other by $(PO_4)^{3-}$ units. Predictions based on the group theory analysis of the non-interacting $(PO_4)^{3-}$ units yield multiply degenerate modes: $1\nu_1$, $2\nu_2$, $3\nu_3$, and $3\nu_4$.[27] The $(PO_4)^{3-}$ has four internal modes of vibration of a tetrahedral ion. Which include: $\nu_1(A_1)$ symmetric stretching, $\nu_3(F_2)$ antisymmetric stretching, $\nu_2(E)$ and $\nu_4(F_2)$ bending vibrations.[28] The Raman spectrum of $GdPO_4$ aligns closely with established data for lanthanide orthophosphates such as $EuPO_4$ and $TbPO_4$. External lattice vibrations are identified at 398 and 419 cm^{-1}, while internal PO_4 bending (ν_2, ν_4) and stretching (ν_1, ν_3) modes appear at 470–630 cm^{-1} and 985–1093 cm^{-1}, respectively. Minor frequency shifts relative to other lanthanide phosphates are attributed to variations in ionic radii and local crystal-field effects.[27–29] The assignment of the Raman spectrum's peaks of $GdPO_4$ powders is listed in Table 4. The low-frequency bands below 450 cm^{-1} originate from lattice vibrations involving Gd^{3+} translations, while the bands between 450 and 650 cm^{-1} are assigned to the ν_2 and ν_4 bending modes of $(PO_4)^{3-}$ tetrahedra. The most intense peak is detected at 985 cm^{-1}, which is attributed to the symmetric stretching P–O vibration ν_1 of the $(PO_4)^{3-}$ tetrahedron. Whereas the additional bands in the range of 1002–1093 cm^{-1} correspond to the asymmetric stretching modes ν_3 of the $(PO_4)^{3-}$ units, indicating the presence of a well-defined tetrahedral geometry and possible slight distortions due to the local crystalline environment. The sharpness and intensity of the observed peaks, particularly in the high-frequency region, suggest a high degree of crystallinity in the synthesized nanoparticles. Furthermore, the absence of broad features typically associated with amorphous phases confirms the formation of a well-ordered $GdPO_4$ structure.[28,30]

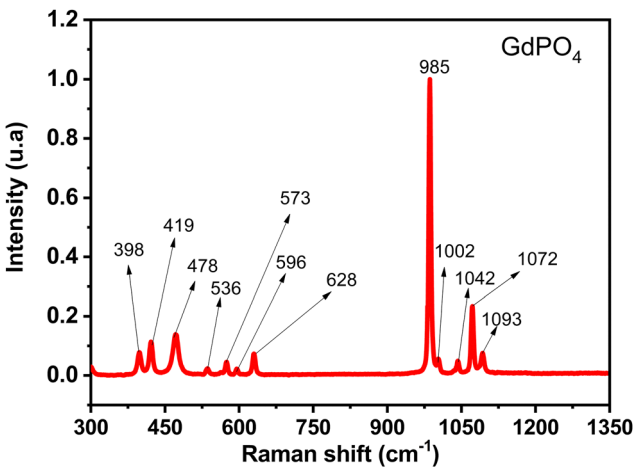

Fig. 2 Raman spectra of $GdPO_4$ nanopowders.

4.2. Experimental optical properties

The optical characteristics of the synthesized $GdPO_4$ were investigated using UV-visible spectroscopy. The corresponding results are analyzed and discussed. Based on Lambert–Beer's law, the measured absorbance A is defined as $A = \log\left(\frac{I_0}{I}\right)$, and it is directly related to the absorption coefficient α through the following expression:

$$\alpha = \frac{2.3026A}{d}$$

where A and d are respectively the absorption and the width of the sample.

The absorption spectrum for $GdPO_4$ is reported in Fig. 3(a). A strong absorption peak is observed at 275 nm. This corresponds to the $^8S_{7/2} \rightarrow {}^6I_J$ transition. Other peaks are observed at 307 and 313 nm, which refer to the $^8S_{7/2} \rightarrow {}^6P_{7/2}$ transition. Both absorption peaks were identified in previous works and reported in.[32]

The optical gap energy E_g^{Opt} is revealed using Tauc's relation:

$$\alpha h\nu = C(h\nu - E_g^{Opt})^t$$

where α denotes the absorption coefficient, $h\nu$ is the photon energy, and C is a material-dependent constant. The exponent t gives a clue about the type of the electronic transition, taking the value of 1/2 for direct allowed transitions and 2 for indirect ones.

Table 4 Observed Raman shift frequencies in (cm^{-1}) for $GdPO_4$, $EuPO_4$ and $TbPO_4$ and their assignment

Vibrational mode	$GdPO_4$ [This work]	$EuPO_4$[27,29]	$TbPO_4$[31]	Assignment
External lattice vibrations	398, 419	189–425	199, 383, 254	Lattice modes
Symmetric O–P–O bending	478	465–477	474	ν_2
Asymmetric O–P–O bending	628	618–634	592, 636	ν_4
Symmetric P–O stretching	985	965–990	993	ν_1
Asymmetric P–O stretching	1072, 1093	1055–1075	1043, 1106	ν_3

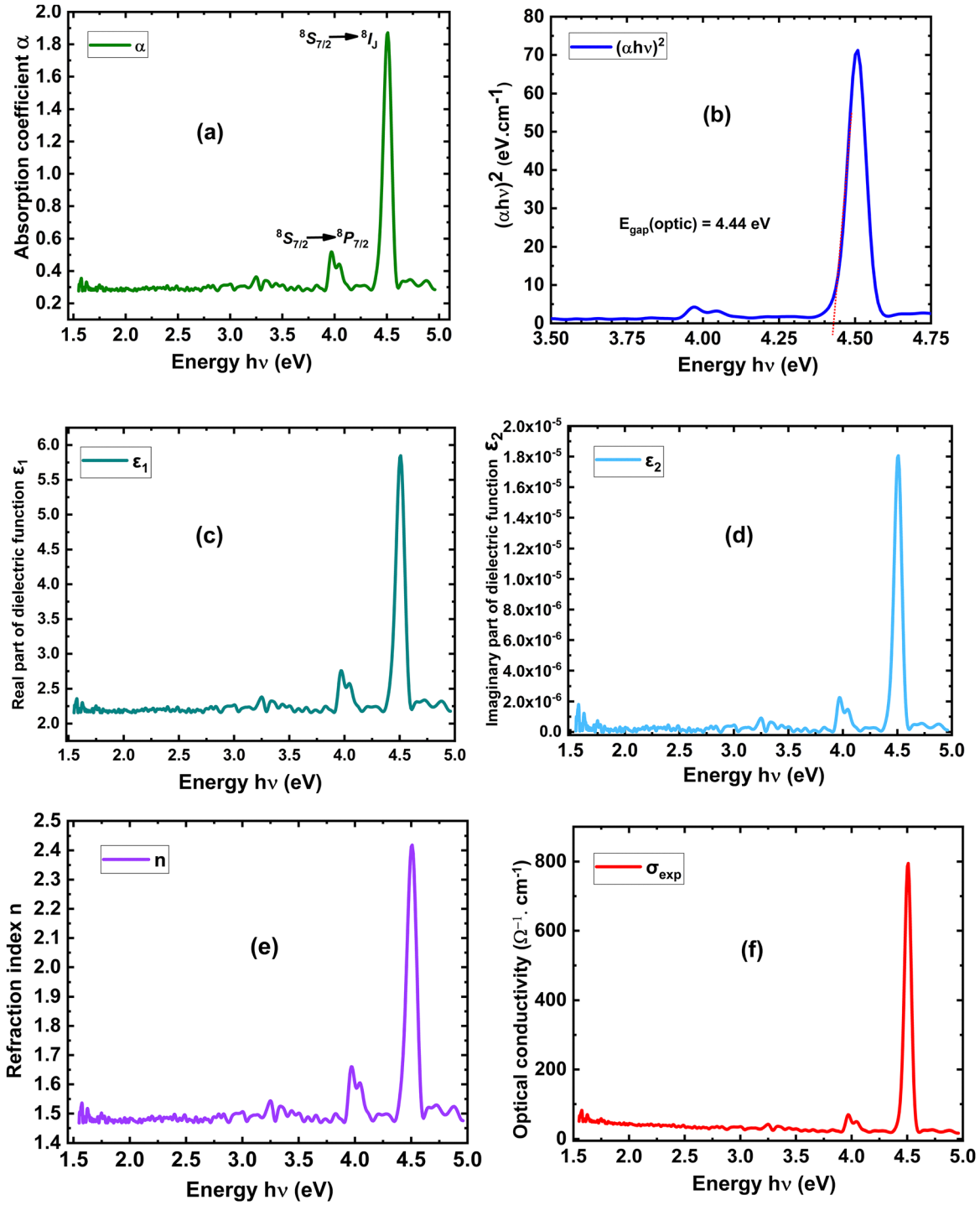

Fig. 3 Experimental optical properties: (a) the experimental absorption coefficient α (λ), (b) the plot of $(\alpha h\nu)^2$ *vs.* $h\nu$, (c) the real part ε_1, (d) the imaginary part ε_2, (e) the refractive index, and (f) the optical conductivity $\sigma(\omega)$.

The optical conductivity, extinction coefficient, and refractive index were calculated using the following formulas:

$$\sigma = \frac{\alpha n c}{4\pi}$$

$$k = \frac{\alpha\lambda}{4\pi}$$

$$n = \frac{1+R}{1-R} + \sqrt{\frac{4R}{(1-R)^2} - k^2}$$

In this study, the $GdPO_4$ powders exhibit a direct band gap; thus, t = 1/2 was used. Fig. 3(b) represents the plot of $(\alpha h\nu)^2$ *versus* $h\nu$, which shows a linear behavior over a significant energy range, confirming the direct transition nature. The

optical gap energy was estimated by extrapolating the linear region of the plot to intercept the photon energy axis, corresponding to $(\alpha h\nu)^2 = 0$. Which corresponds to $E_g^{Opt} = 4.44$ eV. The obtained optical band gap does not correspond to band-to-band transitions. It deals with transitions that take place in the measuring range (250–800 nm) of the UV-vis spectrophotometer, hence only 4f–4f intraconfigurational transitions are captured. The reported value of 4.44 eV does not represent the fundamental electronic band gap. The interconfigurational 4f–5d were captured using a diffuse reflectance spectrophotometer covering a wavelength of (120–300 nm). The electronic band gap of the monazite $GdPO_4$ was reported in a previous study to be 7.8 eV.[33] Due to experimental limitations we could attain energy values greater than 5 eV, which does not allow direct observation of the fundamental band-to-band expected near 8 eV.

The dielectric and optical responses (Fig. 3(c–f)) consistently indicate that the material is a wide-band-gap insulator with localized absorption in the near-UV. The imaginary part ε_2 and the optical conductivity show two peaks at 4.0 eV and 4.5 eV, which produce the corresponding dispersive structure in ε_1 and a strong augmentation of the refractive index n at the same energies. The weak dispersion at energy value 4.0 eV feature is consistent with magnetic-dipole induced intra-4f transitions of Gd^{3+}, while the relatively strong peak at 4.5 eV indicates a transition induced by the same dipole but with higher probability. The optical conductivity $\sigma(\omega)$ is negligible below 4 eV, confirming the insulating behavior. The crests observed at 4 and 4.5 eV are a consequence of the aforementioned transitions $^8S_{7/2} \rightarrow {}^6I_J$ and $^8S_{7/2} \rightarrow {}^8P_{7/2}$, considering their intensities ($<800\ \Omega^{-1}\ cm^{-1}$) and their localized features. We conclude that at this energy range, electrons are not free to conduct.

4.3. Electronic properties

4.3.1. Density of states. To shed light on the electronic structure of our material, we computed the total density of states (DOS) and partial density of states (PDOS) of $GdPO_4$. Precisely, calculations were performed to depict the electronic gap energy, besides the electronic transitions. To depict the contribution of each element included in the material to the electronic properties, partial densities of states (PDOS) are reported in Fig. 4(a)–(d).

Fig. 4(a) and (b) show that the total DOS is dominated mainly by the f orbital of the Gd atom contribution taking

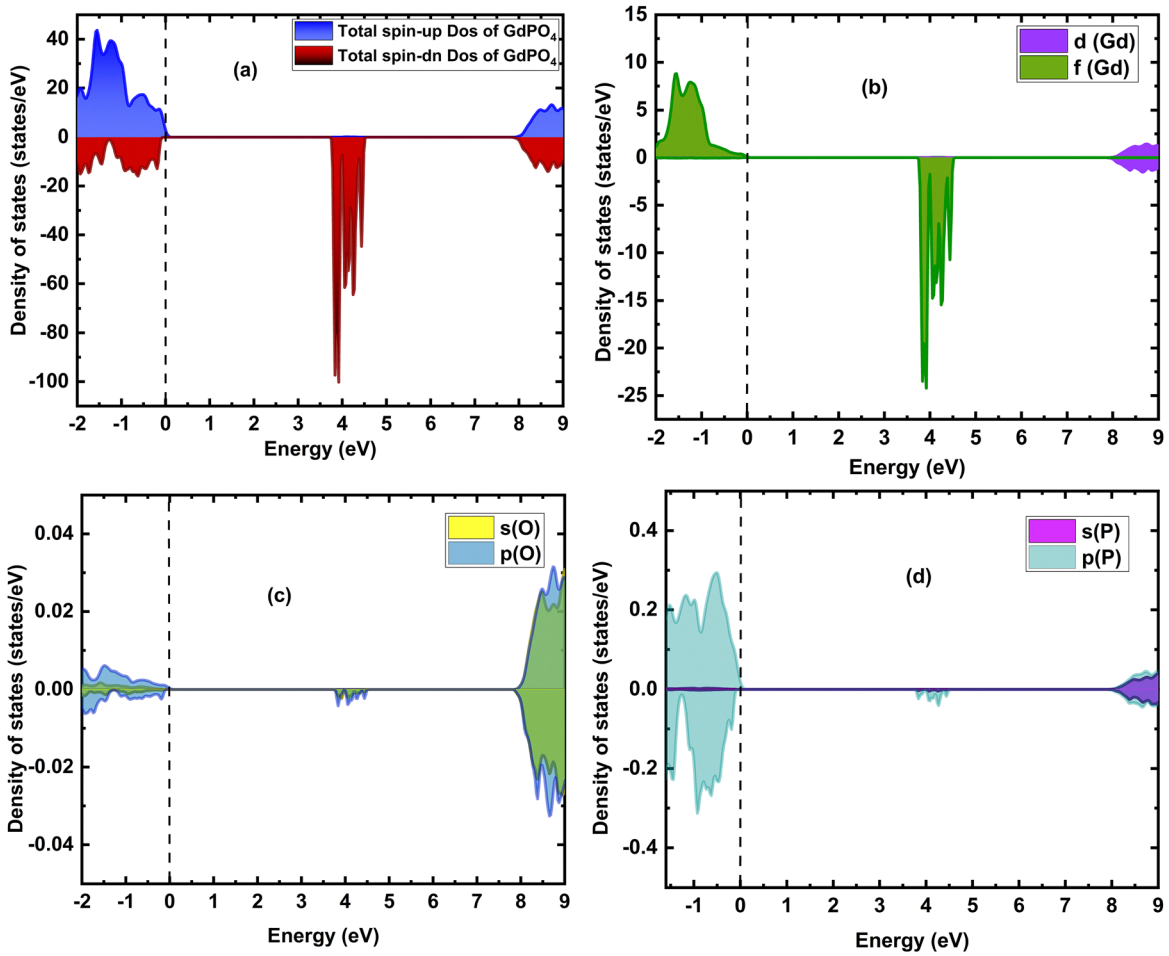

Fig. 4 Total DOS of $GdPO_4$ and partial DOS of gadolinium, oxygen, and phosphorus.

place in both occupied states at negative energy values of spin-up of Gd and unoccupied states contained at negative energy values with major contribution from the spin-down configuration of Gd. In addition, the contribution from spin-up at negative energies resulting from spin–orbit coupling of Gd that takes place in the energy range 4–4.5 eV.

Furthermore, we observe the contribution of the d orbital at energy values around 7.95 eV. It defines the conduction band of the $GdPO_4$. The PDOS of Gd gives evidence of the absence of the contribution from the s orbital to the total Gd PDOS, confirming that this element has lost three electrons. It is in accordance with the rare earth oxidation number 3+. Contribution from phosphorus and oxygen takes place near the Fermi level at negative energies. Partial densities of states of P and O are symmetrical with respect to the *x*-axis, pointing out the non-magnetic behavior of both atoms.

As expected, the $GdPO_4$ is found to be an insulator with a band gap of 8 eV corresponding to the spin-up configuration. The electronic transition from the 4f valence band to the empty 4f states of Gadolinium is forbidden due to the electric-dipole selection rules ($\Delta L = \pm 1$). Nonetheless, it is allowed by the magnetic dipole selection rules ($\Delta L = 0$), particularly for systems having heavy elements including significant spin–orbit coupling. Basically, both initial and final bands of this transition are showing the same parity, $\Delta S = 0$ and $\Delta L = 0$. The 4f–4f transition corresponds to an optical band gap in the range of 4.0–4.4 eV. Electrons that absorb this energy are excited from the valence band (VB) to the 4f excited state; however, they do not contribute to electrical conductivity. Instead, these excited electrons relax back to the VB. Two possible relaxation pathways are radiative relaxation or non-radiative relaxation. We consider the relaxation to be radiative for the following reasons: first, this transition is magnetic-dipole allowed. Secondly, the empty electronic states of 4f (4–4.5 eV) are considered metastable, as can be seen in Fig. 5, 4f empty states occupy flat bands. Thirdly, the empty electronic states of 4f are well separated from the conduction band; a gap of 3.5 eV separates them. We put forward a radiative relaxation pathway of 4 eV. Experimentally, a photon emission at 313 nm (3.96 eV) is observed in the photoluminescence spectrum of $GdPO_4$ under excitation at 254 nm, which is consistent with our analysis.[32]

The computed gap energy matches well the previously published experimental value of 7.8 eV.[33,34] The obtained electronic energy gap using the GGA+mBJ shows better values than the theoretical band gaps obtained by the GGA+U method (5.7 eV) and the hybrid functional HSE06 (6.55 eV).[35]

Furthermore, the Gd atom shows a highly asymmetric DOS, which points to a magnetic behavior with $6.94\mu_B$ as saturation magnetic moment carried by this atom. This finding is consistent with both the experimentally measured magnetic moment ($\mu_{exp} = 7.2 \pm 0.3\mu_B$) and the theoretical free-ion (Gd^{3+}) value ($\mu_{theo} = 7\mu_B$).[12]

4.3.2. Band structures. To provide a more detailed characterization of the electronic structure, the band structures (BS) were also determined. Fig. 5 displays the spin–orbit coupled BS, describing paths between chosen high symmetry points within the first Brillouin zone of the reciprocal lattice of $GdPO_4$. The valence band maximum (VBM) is located at −0.016 eV at the high symmetry point B (0.5; 0; −0.5). The conduction band minimum (CBM) is depicted at an energy level of 7.8 eV at the same high symmetry point. With the knowledge of VBM and CBM locations, we conclude that the monazite $GdPO_4$ has a direct gap energy of 7.8 eV. These conclusions are in good accordance with the abovementioned analysis of the DOS. It is recognized that the localized 4f states in rare-earth compounds are strongly correlated, and their accurate description often requires approaches beyond standard density functional theory. In the present study, the electronic properties were initially

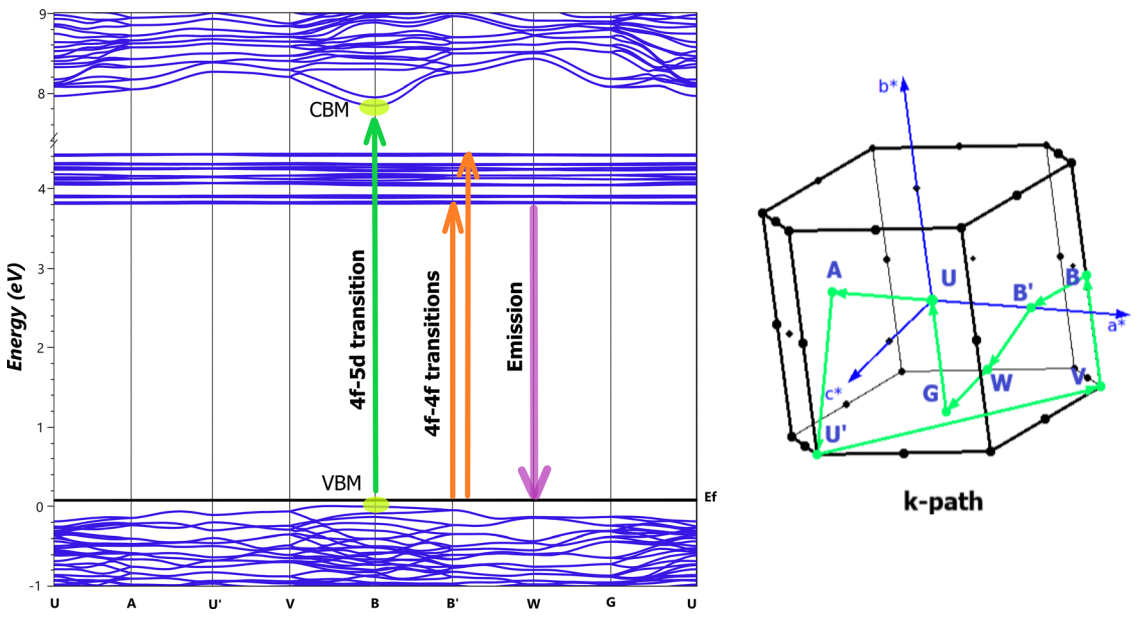

Fig. 5 Band structure of spin-coupled $GdPO_4$.

investigated using the DFT+U and DFT+U+SOC approaches. However, these methods failed to properly reproduce the electronic band gap, yielding values lower than 5 eV and not clearly revealing the intra-configurational 4f–4f transitions. Previous studies have reported similar limitations. For instance, the GGA+U functional significantly underestimates the band gap of $GdPO_4$, showing a value of 5.7 eV, while the hybrid functional HSE06 improves the band gap only moderately (6.55 eV) but still fails to correctly localize the 4f–4f transitions in $GdPO_4$, the absence of 4f bands between VBM and CBM on the $GdPO_4$ shows the inadequacy of the HSE06 framework for studying $LnPO_4$.[35] In addition, the PBEsol functional has been reported to inadequately describe both intra-configurational and inter-configurational transitions in related lanthanide orthophosphates such as $EuPO_4$ and $PrPO_4$.[36] On the other hand, in earlier study on $EuPO_4$ we gave accurate description of both electronic transition types (intraconfigurational 4f–4f and Interconfigurational 4f–5d) using the mBJ+SOC, more precisely authors report a wide electronic band gap of 7.6 eV and three 4f–4f transition are depicted.[37] Consequently, the mBJ potential was adopted in the present work, as it provides a more reliable description of the electronic structure and band gap of wide-band-gap materials. A comparison with other members of the $LnPO_4$ series provides useful insight into the structural and electronic properties of the studied compound. The calculated lattice parameters of $GdPO_4$ (a = 6.6532 Å, b = 6.8491 Å, c = 6.3366 Å, and β = 104.001°) are very close to those reported for $EuPO_4$ (a = 6.6667 Å, b = 6.8649 Å, c = 6.3515 Å, and β = 103.940°), which reflects the similar ionic radii of Eu^{3+} and Gd^{3+} within the monazite structure. In contrast, $TbPO_4$ exhibits slightly different lattice parameters ($a = b$ = 6.940 Å, and c = 6.068 Å) associated with structural variations within the lanthanide orthophosphate family. Concerning the electronic structure, $EuPO_4$ shows an indirect band gap of 7.6 eV with the valence band maximum located at the M_2 point (0.59, 0, −0.19) and the conduction band minimum at Γ (0,0,0). In the present work, $GdPO_4$ exhibits a direct band gap of 7.8 eV occurring at the B high-symmetry point (0.5, 0, −0.5), while $TbPO_4$ also presents a direct transition at the Γ point with a band gap of 5.86 eV. These results highlight the influence of the rare-earth ion on the band structure while preserving the large band gap characteristic of $LnPO_4$ compounds.

4.4. Numerical optical properties

In order to study the optical properties of monazite-structured $GdPO_4$, OPTIC, JOINT, and KRAM programs, as implemented in the Wien2k simulation package, were used. Firstly, the OPTIC program was used to calculate the momentum matrix elements. Then, the JOINT program was used to compute the imaginary part of the dielectric function ε_2. Finally, Kramers–Kronig analysis was carried out using the KRAM program, which is used to deduce the real part of the dielectric tensor ε_1 and compute the optical conductivity and the absorption coefficient.[38] All the calculations were performed corresponding to the photon energy range of 0 to 12 eV. The formulas of the real and imaginary parts of the dielectric function, respectively, are:[38]

$$\varepsilon_{ij(2)}(\omega) = \frac{\hbar^2 e^2}{\pi m^2 \omega^2} \sum_{n,n'} \int_k p_{i;n',n,k} p_{j;n',n,k} \times \left[f\left(\varepsilon_{n,k}\right) - f\left(\varepsilon_{n',k}\right) \right] \delta\left(\varepsilon_{n',k} - \varepsilon_{n,k} - \omega\right)$$

$$\varepsilon_{ij(1)}(\omega) = 1 + \frac{2}{\pi} P \int_0^\infty \frac{\omega' \varepsilon_{ij(2)}(\omega')}{\omega'^2 - \omega^2} \mathrm{d}\omega'$$

Additionally, with the Knowledge of the complex dielectric tensor $\varepsilon = \varepsilon_1 + i\varepsilon_2$, the refractive index, extinction coefficient, and optical conductivity were calculated using the following formulas:

$$k = \frac{\sqrt{2}}{2} \left[\sqrt{\varepsilon_1{}^2 + \varepsilon_2{}^2} - \varepsilon_1 \right]^{1/2}$$

$$n = \frac{\sqrt{2}}{2} \left[\sqrt{\varepsilon_1{}^2 + \varepsilon_2{}^2} + \varepsilon_1 \right]^{1/2}$$

$$\alpha = \frac{2\omega k}{cn}$$

$$\sigma = \frac{\alpha n c}{4\pi}$$

Fig. 6(a) and (b) illustrate the absorption coefficient $\alpha(\omega)$ and optical conductivity $\sigma(\omega)$. The absorption coefficient $\alpha(\omega)$ reflects the material's capacity to absorb incident photons having specific energies. The absorption spectra were also analyzed along the three principal crystallographic directions. As depicted in Fig. 6(a), no significant absorption phenomena are observed below 4 eV, aligning well with the computed band structure. Beyond this energy threshold, $\alpha(\omega)$ shows a minor broad peak from 4 to 5.2 eV. This slight contribution is due to the intra-configurational 4f–4f transition. This electronic transition is reasonable and known to be very small in intensity (1–60 cm^{-1}) in comparison to the 4f–5d transitions, owing to the nature of magnetic–dipole transitions.[39] The reversed electronic transition is the origin of luminescence properties in $GdPO_4$.[2] The intra-configurational transition is observed in previous band structure calculations on lanthanide-based orthophosphate and experimental optical studies.[2,40] Beyond the energy value of 8 eV, $\alpha(\omega)$ increases drastically, showing an absorption edge in the ultraviolet region for all the crystallographic directions and reaches its peak near 11.5 eV. The calculated absorption spectrum reproduces the transparency of $GdPO_4$ across the visible range and predicts a fundamental interband absorption edge in the deep-UV at 8 eV, where the absorption coefficient exceeds 10^5 cm^{-1}. In the 4–5.2 eV window, theory yields weak features that we assigned to intra-4f transitions of Gd^{3+}, in agreement with the experimental spectrum, which displays the $^8S_{7/2} \rightarrow {}^6P_{7/2}$ (4.0 eV) and a pronounced $^8S_{7/2} \rightarrow {}^6I_J$ (4.5 eV) band. The absence of an interband onset in the measured data is attributed to the limited spectral range of the utilized spectrophotometer

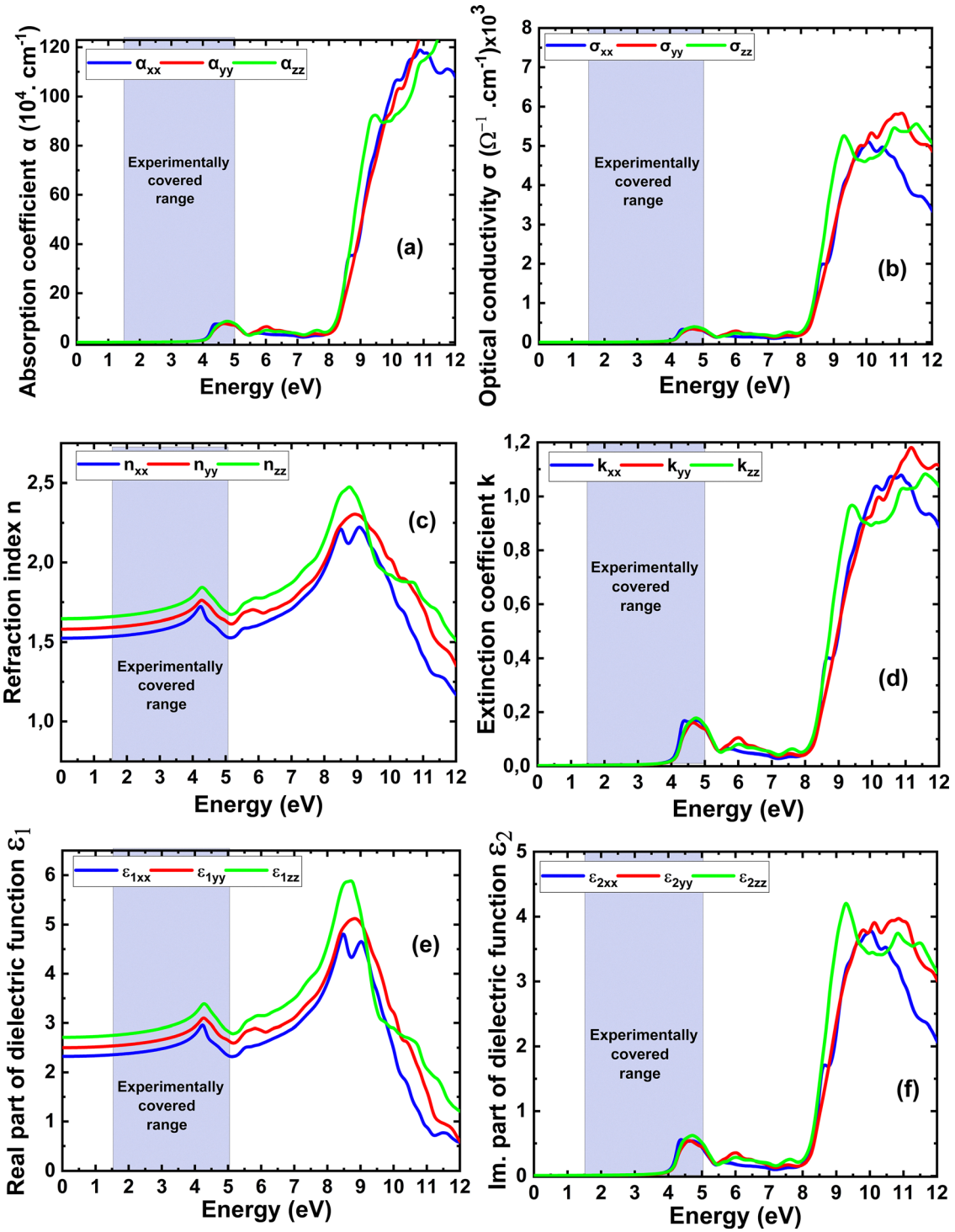

Fig. 6 Absorption coefficient (a), optical conductivity (b), refractive index $n(\omega)$ (b), extinction coefficient $k(\omega)$ (c), $\varepsilon_1(\omega)$, the real part (e), and imaginary $\varepsilon_2(\omega)$ part (f) of the complex dielectric function $\varepsilon(\omega)$ of $GdPO_4$.

($\leq$5 eV); measurements extending into the vacuum ultra-visible (VUV) would be required to observe the theoretical edge. Minor discrepancies in the intensity and sharpness of the 4f lines likely arise from the broadening parameter during calculation, where we assume that two peaks overlapped to give a bump-like feature in the energy range 4–5.2 eV. Overall, the combined results establish $GdPO_4$ as a wide band gap insulator with localized 4f absorptions in the near-UV region and a fundamental gap located in the deep-UV region.

The optical conductivity $\sigma(\omega)$ represents the generation of conduction band electrons upon interaction with incident photons of specific energy. Similar to the absorption, the onset

of optical conductivity occurs at the band gap energy. The small observed values (300 Ω^{-1} cm^{-1}) in the energy range of 4–5.2 eV are a sign of inter-band transitions. A pronounced peak is observed around 12 eV for the *zz* direction, indicating strong optical transitions in the ultraviolet region of the electromagnetic spectrum. On the other hand, a delayed strong peak is observed at energy values of 10.5 and 11 eV for *xx* and *yy* directions.

Fig. 6(c and d) illustrate the refractive index $n(\omega)$ and the extinction coefficient $k(\omega)$. The simulated refractive indexes of $n(xx)$, $n(yy)$, and $n(zz)$ are 1.51, 1.57, and 1.64 eV, respectively, which is closer to the experimental value 1.76 eV reported for Nd doped $GdPO_4$.[41] This is also in good agreement with a previous theoretical study 1.55–1.63.[20] We notice two peaks, the first is around the 4f–4f transition peak (4 eV), where *n* has reached 1.8. The second strong peak depicted at 8.5 eV is due to the 4f–5d transition, which is known to have a higher probability, where *n* has reached a value of 2.5. The extinction coefficient $k(\omega)$ shows a bump at an energy range of 4–5 eV, then it starts to rise at the band gap energy, displaying a prominent peak within the 9.5–12 eV energy range. This peak coincides with that of the imaginary part of the dielectric function $\varepsilon_2(\omega)$, indicating efficient photon absorption in this spectral region.

The simulated spectra of the real $\varepsilon_1(\omega)$ and imaginary $\varepsilon_2(\omega)$ parts of the complex dielectric function $\varepsilon(\omega)$ of $GdPO_4$ are illustrated in Fig. 6(e) and (f). The dielectric function $\varepsilon(\omega)$ is calculated for the polarized incident radiations along the *xx*, *yy*, and *zz* directions for the purpose of examining the optical anisotropy. It is seen from Fig. 6(e) and (f) show that both the real and imaginary dielectric functions under the three directions do not coincide, demonstrating a minor optical anisotropy. From the dispersion curve of the real part, a progressive increase from the static values of $\varepsilon_1(\omega)$ is shown: ε_1 = 2.3 along *xx*, ε_1 = 2.5 along *yy*, and ε_1 = 2.6 along *zz*. Following the initial jump, $\varepsilon_1(\omega)$ reaches a maximum value for each direction at energy values of 8.5 eV, 8.8 eV, and 8.5 eV, respectively, for *xx*, *yy*, and *zz* directions. Beyond this, $\varepsilon_1(\omega)$ starts to decrease progressively. The imaginary part of the dielectric function ε_2 designates the absorption and emission of light. It represents the transitions of electrons between occupied and unoccupied states. Every single peak describes a transition. The ε_2 curve gives a clear value of the energy gap of the material, which is depicted at 8 eV; another peak is observed at 4 eV, the latter designates the emission, which is congruent with results from the electronic structure and experimental studies.

The experimentally obtained ε_2 values are lower than the simulated values. This is due to the difference in the nature of the intrinsic response of an ideal, dense single crystal. Conversely, the experimental data come from a powder sample. The random orientation of the anisotropic crystallites induces an average dielectric tensor, and, more importantly, the high porosity causes significant light scattering. This scattering considerably reduces the apparent amplitude of the measured ε_2, thus explaining the order-of-magnitude difference between the measured and calculated signal intensity.

5. Conclusion

Our combined DFT and spectroscopic study accurately characterizes $GdPO_4$ as a wide-bandgap optical material, demonstrating the correctness of the fitted theoretical framework and providing a reliable reference for the bandgap estimation on lanthanide-based phosphates and luminescence property tuning for future applications in photonics, scintillation, and biomedical imaging. Rietveld analysis showed that the solid-state synthesized $GdPO_4$ crystallizes in the monoclinic space group $P2_1/n$. Experimentally, the UV-vis absorption spectrum revealed two distinct peaks at 275 and 303 nm. These peaks correspond to the 4f–4f transitions characteristic of the Gd^{3+} ion. The fundamental band edge could not be depicted since it surpasses the operational spectral limits (1.5–5.4 eV) of the spectrophotometer. In the theoretical analysis, using the mBJ+SOC framework, we determined the direct electronic bandgap of the $GdPO_4$ monazite crystal to be 7.8 eV, corresponding to the $4f^{n-1}$ $5d^1$ transition. This value is consistent with other rare-earth orthophosphate systems and a more accurate prediction obtained with GGA+U and the HSE06 hybrid functional. Intraconfigurational 4f–4f transitions were identified by DFT and analyzed in terms of amplitude and intensity. Our study provides accurate predictions of the energy levels of $GdPO_4$ and the possible radiative emission energy, which is equal to 3.96 eV, based on DOS and band structure calculations. This analysis presents a novelty. Finally, the magnetic moment calculated for the gadolinium (Gd) atom was 6.86μ_B, which is in good accordance with the experimentally measured magnetic moment of 7.2 $\pm$ 0.3μ_B. This combined study permits a deeper comprehension of electronic transition types in lanthanide-based phosphors and provides the scientific community with a robust basis for tuning of new luminescent materials.

Conflicts of interest

The authors declare that they have no known competing financial interests or personal relationships that could have appeared to influence the work reported in this paper.

Data availability

Data will be made available on request.

Supplementary information (SI) is available. See DOI: https://doi.org/10.1039/d6ma00117c.

References

1 S. N. Achary, S. Bevara and A. K. Tyagi, Recent progress on synthesis and structural aspects of rare-earth phosphates, *Coord. Chem. Rev.*, 2017, **340**, 266–297, DOI: 10.1016/j.ccr.2017.03.006.

2 S. K. Sharma, J. Beyer, R. Gloaguen and J. Heitmann, Non-quenching photoluminescence emission up to at least 865 K upon near-UV excitation in a single crystal of orange-red

emitting $SmPO_4$, *Phys. Chem. Chem. Phys.*, 2019, **21**, 25669–25677, DOI: 10.1039/C9CP05663G.

3 N. Huittinen, Y. Arinicheva, M. Schmidt, S. Neumeier and T. Stumpf, Using Eu^{3+} as an atomic probe to investigate the local environment in $LaPO_4$–$GdPO_4$ monazite end-members, *J. Colloid Interface Sci.*, 2016, **483**, 139–145, DOI: 10.1016/j.jcis.2016.08.027.

4 S. K. Sharma, T. Köhler, J. Beyer, M. Fuchs, R. Gloaguen and J. Heitmann, Extending the temperature sensing range using Eu^{3+} luminescence up to 865 K in a single crystal of $EuPO_4$, *Phys. Chem. Chem. Phys.*, 2019, **21**, 16329–16336, DOI: 10.1039/C9CP03501J.

5 S. K. Sharma, J. Beyer, R. Gloaguen and J. Heitmann, Comparing the optical properties and thermal stability of green ($TbPO_4$), yellow ($DyPO_4$), and red ($PrPO_4$) emitting single crystal samples, *Phys. Chem. Chem. Phys.*, 2020, **22**, 10247–10255, DOI: 10.1039/D0CP01561J.

6 M. L. Williams, M. J. Jercinovic and C. J. Hetherington, Microprobe Monazite Geochronology: Understanding Geologic Processes by Integrating Composition and Chronology, *Annu. Rev. Earth Planet. Sci.*, 2007, **35**, 137–175, DOI: 10.1146/annurev.earth.35.031306.140228.

7 A. Lempicki, E. Berman, A. J. Wojtowicz, M. Balcerzyk and L. A. Boatner, Cerium-doped orthophosphates: new promising scintillators, *IEEE Trans. Nucl. Sci.*, 1993, **40**, 384–387, DOI: 10.1109/23.256585.

8 P. Laporta, S. Taccheo, S. Longhi, O. Svelto and C. Svelto, Erbium–ytterbium microlasers: optical properties and lasing characteristics, *Opt. Mater.*, 1999, **11**, 269–288, DOI: 10.1016/S0925-3467(98)00049-4.

9 S. Neumeier, Y. Arinicheva, Y. Ji, J. M. Heuser, P. M. Kowalski, P. Kegler, H. Schlenz, D. Bosbach and G. Deissmann, New insights into phosphate based materials for the immobilisation of actinides, *Radiochim. Acta*, 2017, **105**, 961–984, DOI: 10.1515/ract-2017-2819.

10 R. C. Ewing and L. Wang, Phosphates as Nuclear Waste Forms, *Rev. Mineral. Geochem.*, 2002, **48**, 673–699, DOI: 10.2138/rmg.2002.48.18.

11 S. Rodriguez-Liviano, A. I. Becerro, D. Alcántara, V. Grazú, J. M. De La Fuente and M. Ocaña, Synthesis and Properties of Multifunctional Tetragonal Eu:$GdPO_4$ Nanocubes for Optical and Magnetic Resonance Imaging Applications, *Inorg. Chem.*, 2013, **52**, 647–654, DOI: 10.1021/ic3016996.

12 M. Lassri, S. El Ouahbi, I. Abdelrhafore, L. E. Hachemi Omari, A. El Hachmi, H. Hamouda, B. Harradi, Y. Ounza, G. Viscusi, C. Minaud, C. Jama and H. Lassri, Large reversible magnetocaloric effect in $GdPO_4$ nano-spherical particles at ultralow temperatures, *J. Magn. Magn. Mater.*, 2025, 173291, DOI: 10.1016/j.jmmm.2025.173291.

13 J. Fang, B. Pan, X. Hu, N. Yu, M. Pan, H. Ge, H. Yang and Q. Wu, Giant Magnetocaloric Effect and Magnetic Critical Behavior in Polycrystalline $GdPO_4$, *J. Supercond. Nov. Magn.*, 2025, **38**, 13, DOI: 10.1007/s10948-024-06866-8.

14 Y. Y. Yu, D. N. Petrov, K. C. Park, B. T. Huy and P. T. Long, Magnetic and cryogenic magnetocaloric properties of $GdPO_4$ nanorods, *J. Magn. Magn. Mater.*, 2021, **519**, 167452, DOI: 10.1016/j.jmmm.2020.167452.

15 Y. Li, J. Wang, H. Huang, J. Wang, M. Zhang and Mm Liang, Co-coating effect of $GdPO_4$ and carbon on $LiFePO_4$ cathode surface for lithium ion batteries, *Adv. Powder Technol.*, 2019, **30**, 1442–1449, DOI: 10.1016/j.apt.2019.04.017.

16 Y. Li, Q. Ren, W. Xu, H. Huang, L. Chen, Y. Fu, J. Wang and Z. Wang, Surface stabilized Ni-rich $LiNi_{0.9}Co_{0.08}Al_{0.02}O_2$ cathode materials via surface modification with $GdPO_4$ for lithium-ion batteries, *Solid State Ionics*, 2023, **403**, 116397, DOI: 10.1016/j.ssi.2023.116397.

17 J. P. Perdew, K. Burke and M. Ernzerhof, Generalized Gradient Approximation Made Simple, *Phys. Rev. Lett.*, 1996, **77**, 3865–3868, DOI: 10.1103/PhysRevLett.77.3865.

18 K. Schwarz, P. Blaha and G. K. H. Madsen, Electronic structure calculations of solids using the WIEN2k package for material sciences, *Comput. Phys. Commun.*, 2002, **147**, 71–76, DOI: 10.1016/S0010-4655(02)00206-0.

19 P. Novák, F. Boucher, P. Gressier, P. Blaha and K. Schwarz, Electronic structure of the mixed valence system (YM)2 $BaNiO_5$ (M = Ca, Sr), *Phys. Rev. B: Condens. Matter Mater. Phys.*, 2001, **63**, 235114, DOI: 10.1103/PhysRevB.63.235114.

20 F. Tran and P. Blaha, Accurate Band Gaps of Semiconductors and Insulators with a Semilocal Exchange-Correlation Potential, *Phys. Rev. Lett.*, 2009, **102**, 226401, DOI: 10.1103/PhysRevLett.102.226401.

21 S. Gates-Rector and T. Blanton, The Powder Diffraction File: a quality materials characterization database, *Powder Diffr.*, 2019, **34**, 352–360, DOI: 10.1017/S0885715619000812.

22 T. Degen, M. Sadki, E. Bron, U. König and G. Nénert, The HighScore suite, *Powder Diffr.*, 2014, **29**, S13–S18, DOI: 10.1017/S0885715614000840.

23 D. Louër and A. Boultif, Some further considerations in powder diffraction pattern indexing with the dichotomy method, *Powder Diffr.*, 2014, **29**, S7–S12, DOI: 10.1017/S0885715614000906.

24 H. M. Rietveld, A profile refinement method for nuclear and magnetic structures, *J. Appl. Crystallogr.*, 1969, **2**, 65–71, DOI: 10.1107/S0021889869006558.

25 J. Rodríguez-Carvajal, Recent advances in magnetic structure determination by neutron powder diffraction, *Phys. B*, 1993, **192**, 55–69, DOI: 10.1016/0921-4526(93)90108-I.

26 T. Hahn, *International tables for crystallography*, 5th edn, Kluwer academic publ, Dordrecht, 2002.

27 E. N. Silva, A. P. Ayala, I. Guedes, C. W. A. Paschoal, R. L. Moreira, C.-K. Loong and L. A. Boatner, Vibrational spectra of monazite-type rare-earth orthophosphates, *Opt. Mater.*, 2006, **29**, 224–230, DOI: 10.1016/j.optmat.2005.09.001.

28 G. M. Begun, G. W. Beall, L. A. Boatner and W. J. Gregor, Raman spectra of the rare earth orthophosphates, *J. Raman Spectrosc.*, 1981, **11**, 273–278, DOI: 10.1002/jrs.1250110411.

29 J. Heuser, A. A. Bukaemskiy, S. Neumeier, A. Neumann and D. Bosbach, Raman and infrared spectroscopy of monazite-type ceramics used for nuclear waste conditioning, *Prog. Nucl. Energy*, 2014, **72**, 149–155, DOI: 10.1016/j.pnucene.2013.09.003.

30 N. K. Sahu, R. S. Ningthoujam and D. Bahadur, Disappearance and recovery of luminescence in $GdPO_4$:Eu^{3+} nanorods: Propose to water/OH• release under near infrared and gamma irradiations, *J. Appl. Phys.*, 2012, **112**, 014306, DOI: 10.1063/1.4731644.
31 Z. Khadraoui, K. Horchani-Naifer, M. Ferhi and M. Ferid, Electronic structure and optical properties of $TbPO_4$: Experiment and density functional theory calculations, *Opt. Mater.*, 2015, **47**, 484–489, DOI: 10.1016/j.optmat.2015.06.025.
32 S. K. Sharma, Evidence of thermal ionization induced luminescence quenching in $CePO_4$ and $GdPO_4$, *Mater. Adv.*, 2023, **4**, 157–163, DOI: 10.1039/D2MA00951J.
33 E. Nakazawa and F. Shiga, Vacuum ultraviolet luminescence-excitation spectra of RPO_4: Eu^{3+} (R = Y, La, Gd and Lu), *J. Lumin.*, 1977, **15**, 255–259, DOI: 10.1016/0022-2313(77)90024-2.
34 T. Lyu and P. Dorenbos, Charge carrier trapping processes in lanthanide doped $LaPO_4$, $GdPO_4$, YPO_4, and $LuPO_4$, *J. Mater. Chem. C*, 2018, **6**, 369–379, DOI: 10.1039/C7TC05221A.
35 Z. Khadraoui, K. Horchani-Naifer, M. Ferhi and M. Ferid, The density functional study of electronic structure and optical properties of gadolinium monophosphate, *Chin. J. Phys.*, 2019, **59**, 333–339, DOI: 10.1016/j.cjph.2019.02.025.
36 J. Li, J. Liu, Y. Zhang, W. Sun, Y. Wang, H. Wu, L. Li, C. Cheng, Y. Wang, K. Tan and F. Liu, Exploring the Ln–O bonding nature and charge characteristics in monazite in relation to microwave dielectric properties, *J. Am. Ceram. Soc.*, 2024, **107**, 175–187, DOI: 10.1111/jace.19402.
37 I. Abdelrhafor, L. H. Omari, M. Lassri, L. Abbassi, A. El Hachmi, S. Tarik, V. Tuyikeze, H. Lassri, E. K. Hlil and M. Chafi, Structural, optical, and electronic properties of europium orthophosphate: a combination of experimental and theoretical studies, *J. Mater. Chem. C*, 2026, **14**(11), 4598–4607, DOI: 10.1039/d5tc03857j.
38 C. Ambrosch-Draxl and J. O. Sofo, Linear optical properties of solids within the full-potential linearized augmented planewave method, *Comput. Phys. Commun.*, 2006, **175**, 1–14, DOI: 10.1016/j.cpc.2006.03.005.
39 K. Mori, H. Nishimura, M. Nakayama and H. Ishibashi, Dynamical aspects of the core excitons formed by the 4f–4f transitions of Gd^{3+} in Gd_2SiO_5, *J. Lumin.*, 2000, **87–89**, 266–268, DOI: 10.1016/S0022-2313(99)00310-5.
40 Z. Khadraoui, K. Horchani-Naifer, M. Ferhi and M. Ferid, Electronic structure and optical properties of $TbPO_4$: Experiment and density functional theory calculations, *Opt. Mater.*, 2015, **47**, 484–489, DOI: 10.1016/j.optmat.2015.06.025.
41 N. Ben Amar, T. Kallel, T. Koubaa, M. A. Hassairi, M. Dammak and E. Cavalli, Synthesis, characterization and optical spectroscopy of $GdPO_4$:Er^{3+}, *Luminescence*, 2020, **35**, 1056–1067, DOI: 10.1002/bio.3817.